Promotion Effect of Ce Doping on Catalytic Performance of LaMnO₃ for CO Oxidation

Nan Wang, Shan Wang, Jie Yang, Ping Xiao and Junjiang Zhu *

College of Chemistry and Chemical Engineering, Wuhan Textile University Chemistry, Wuhan 430200, China
* Correspondence: jjzhu@wtu.edu.cn

Abstract: In this paper, Ce-doped $La_{1-x}Ce_xMnO_3$ perovskite catalysts are prepared by the sol–gel method, and the promotion effect of Ce doping on $LaMnO_3$ catalysts for CO oxidation is investigated. The catalysts are characterized by X-ray diffractograms, Raman, N_2 physisorption isotherms, temperature-programed reduction with H_2, transmission electron microscopy, and X-ray photoelectron spectroscopy. The results show that the Ce doping greatly improves the catalytic activity of $LaMnO_3$ for CO oxidation. Among the $La_{1-x}Ce_xMnO_3$ catalysts, $La_{0.8}Ce_{0.2}MnO_3$ shows the best CO catalytic activity, with 100% CO conversion obtained at 180 °C. The characteristic results show that the $LaMnO_3$ perovskite phase exists in all Ce-doped catalysts, and the CeO_2 crystalline phase begins to appear at $x \geq 0.1$. The high activity of $La_{0.8}Ce_{0.2}MnO_3$ for CO oxidation could be that: (1) it possesses large surface area (25.8 m^2/g) to contact with reactants; (2) it has a high surface $Ce^{3+}/(Ce^{3+} + Ce^{4+})$ ratio of 0.27, which means high content of oxygen vacancies used for O_2 adsorption and activation; and (3) it exhibits strong reducibility that is beneficial to CO activation.

Keywords: perovskite oxide; $LaMnO_3$; Ce doping; CO oxidation

1. Introduction

With the continuous improvement of people's living standards, the number of fuel vehicles is increasing. Carbon monoxide (CO), as a main component of the automobile exhaust, causes serious pollution problems [1,2]. It is hard to react with other substances in the atmosphere, and thus it will directly affect the climate and environment [3–5]. Besides, when excessive CO is inhaled into the human body, it will damage the cardiovascular and nervous systems, leading to headache, syncope, and even death [6]. At present, the most common and efficient means of treating CO pollutants is catalytic oxidation, and the core of this technology is a catalyst with high catalytic activity [7].

According to the compositions, the catalysts can be divided into noble metal and non-noble metal catalysts [8]. Because noble metal is scarce and expensive, the non-noble metal catalysts receive broader application prospects in terms of cost and sustainability. Perovskite, as a typical representative of non-noble metal catalysts, is one of the alternative materials to replace noble metal catalysts owing to its simple synthesis, low cost, good catalytic performance, and wide application prospect in various catalytic reactions. In addition, perovskite oxides also have good inclusivity, so that their structural properties can be regulated by doping other elements to achieve the purpose of application [9].

The general chemical formula of perovskite-type oxides can be expressed as ABO_3, where A is a typical lanthanide, alkali metal, or alkaline earth metal cation with large ionic radius; and B is a transition metal cation with small ionic radius, such as Mn, Co, Fe, Ni, Cr, or Ti [10]. The B-site metal plays fundamental role in catalysis, while the A-site metal is mainly to support and stabilize the perovskite structure [11]. The substitution of A- or B-site cation with a foreign one can change the composition and valence state of the B-site metal, while remaining structurally undestroyed [12]. Therefore, perovskite-type metal oxides are widely applied in catalytic reactions, including the CO oxidation. Among

the numerous perovskite-type metal oxides, lanthanum-containing manganate ($LaMnO_3$) attracts increasing attention due to its multifunctional catalytic performances and chemical stability, especially as a low-cost alternative to the noble metal for CO oxidation [13,14].

Tei ji Nakamuya et al. [15] studied the oxidation performance of $La_{1-x}Sr_xMnO_3$ catalyst for CO removal, showing that with the increase in Sr substitution, the oxidation performance of the catalyst improves, while the re-reduction rate decreases. Peng et al. [16,17] prepared $La_{0.8}K_{0.2}Mn_{1-x}Cu_xO_3$ catalysts and found that the simultaneous substitution of cations at A and B sites could not only convert Mn^{3+} to Mn^{4+}, but also generate oxygen vacancies, thereby improving the reaction activity. In previous works, it was reported that the Ce doping can increase the surface area, oxygen storage capacity, and, hence, the CO removal efficiency [18]. For example, Gao et al. [19] found that the Ce doping increases the surface area and reduces the grain size of $La_{1-x}Ce_xCoO_3$, thus improving the CO oxidation activity. Xiang et al. [20] found that Ce^{4+} in $La_{1-x}Ce_xFeO_3$ strengthens the interaction between the catalyst and the adsorbed O_2, facilitating the activation of O–O bonds, thereby accelerating the reaction rate. Mathieu-Deremince et al. [21] conduct CO oxidation on $La_{1-x}Ce_xBO_3$ (B = Ti, Cr, Mn, Fe, Ni, Co) and found that the introduction of Ce^{4+} reduces the oxidation state of Mn ions at the B site, which improves the surface area of the catalyst.

The $LaMnO_3$ catalyst has remarkable CO catalytic oxidation activity. However, it has not received actual industrial application yet, and its oxygen storage capacity needs to be further optimized. Since the Ce doping can bring more oxygen and facilitate oxygen mobilization, it would be of interest to clarify the influence of Ce doping on the oxygen storage capacity and CO oxidation activity of the $LaMnO_3$ catalyst. The results of which would then provide new ideas to modify perovskite oxides for catalysis use.

In this work, a series of Ce-doped $La_{1-x}Ce_xMnO_3$ perovskites were prepared for a CO oxidation reaction. X-ray diffractograms (XRD), Raman, transmission electron microscopy (TEM), N_2 physisorption isotherms, X-ray photoelectron spectroscopy (XPS), and temperature-programed reduction with H_2 (H_2-TPR) were used to study the effects of Ce doping on the catalytic performances of $LaMnO_3$ for CO oxidation. The results showed that $LaMnO_3$ with 20% Ce doping at the La site, i.e., $La_{0.8}Ce_{0.2}MnO_3$, has the largest surface area, abundant oxygen vacancies, and strong reducibility among the $La_{1-x}Ce_xMnO_3$ catalysts ($0 \leq x \leq 0.25$), and, hence, exhibited the highest activity for CO oxidation.

2. Results and Discussion

2.1. Catalytic Performance

Figure 1 shows the catalytic activity of $La_{1-x}Ce_xMnO_3$ ($0 \leq x \leq 0.25$) for CO oxidation as a function of temperature. The conversion curves of all catalysts are similar, and the activity increases with the reaction temperature. For $LaMnO_3$, the activity slowly increases in the temperature range of $60-140$ °C, and only 9% CO conversion was obtained at 140 °C. After the doping of Ce atoms, the activity of $La_{1-x}Ce_xMnO_3$ showed a trend of, first, increase, and then decrease, with the best activity obtained from $La_{0.8}Ce_{0.2}MnO_3$, which exhibits 100% CO conversion at 180 °C. The activity $La_{1-x}Ce_xMnO_3$ is better than that of $LaMnO_3$. This could be that the Ce doping induces the formation of oxygen vacancies, resulting in charge imbalance on the surface of the catalyst, which makes it easier to adsorb oxygen and promotes the oxidation of CO.

To compare other doping catalysts and indicate the superiority $La_{0.8}Ce_{0.2}MnO_3$ for CO oxidation, a series of $LaMnO_3$-based catalysts, reported in studies, are compared and shown in Table 1. For substitution of the A-site cation, $La_{0.4}Sr_{0.6}MnO_3$ [22], was shown to have a smaller BET surface area than that of $La_{0.8}Ce_{0.2}MnO_3$. A similar result was obtained for the CO oxidation activity. The substitution of the B-site cation, $LaMn_{0.8}Fe_{0.2}O_3$ [23], obtained 50% CO conversion and 100% CO conversion at 135 °C and 163 °C, respectively, which are slightly lower results than that of $La_{0.8}Ce_{0.2}MnO_3$; $LaAl_{0.8}Mn_{0.2}O_3$ [24] exhibits almost the same BET surface area, showing better low-temperature activity but less high-temperature activity than that of $La_{0.8}Ce_{0.2}MnO_3$. The noble metal loading catalyst,

2 wt% Au-LaMnO$_3$ [25], shows relatively higher temperature to obtain 50% and 100% CO conversion than that of La$_{0.8}$Ce$_{0.2}$MnO$_3$.
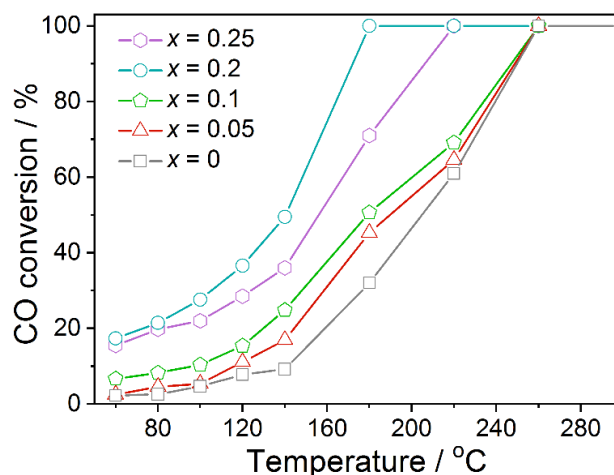

Figure 1. CO conversions obtained from the La$_{1-x}$Ce$_x$MnO$_3$ ($0 \leq x \leq 0.25$) catalysts as a function of reaction temperature.

Table 1. Comparison of BET surface area and CO conversion with other reported works.

Catalyst	BET Surface Area (m^2/g)	Reaction Conditions	CO Conversion		Reference
			T$_{50}$ (°C)	T$_{100}$ (°C)	
La$_{0.8}$Ce$_{0.2}$MnO$_3$	25.8	0.5% CO and 6.5% O$_2$; WHSV = 30,000 mL/(g·h)	140	180	This work
La$_{0.4}$Sr$_{0.6}$MnO$_3$	12.0	1.0% CO and 10.0% O$_2$; WHSV = 90,000 mL/(g·h)	135	163	[22]
LaMn$_{0.8}$Fe$_{0.2}$O$_3$	55.7	1.0% CO and 1.25%/O$_2$; GHSV = 12,000 h^{-1}	187	200	[23]
LaAl$_{0.8}$Mn$_{0.2}$O$_3$	25.0	1% CO and 20% O$_2$; GHSV = 12,000 h^{-1}	127	227	[24]
2 wt% Au-LaMnO$_3$	17.7	2300 ppm CO and 7% O$_2$; WHSV = 30,000 mL/(g·h)	234	290	[25]

2.2. XRD and Raman Results

Figure 2a shows the XRD patterns of La$_{1-x}$Ce$_x$MnO$_3$. Diffraction peaks at 2θ = 22.9°, 32.6°, 40.2°, 46.8°, 52.7°, 58.2°, 68.3°, and 77.8° that are attributed to LaMnO$_3$ (PDF#75-0440) are observed in all samples, indicating that LaMnO$_3$ is the main composition of La$_{1-x}$Ce$_x$MnO$_3$. For LaMnO$_3$ and La$_{0.95}$Ce$_{0.05}$MnO$_3$, no diffraction peaks, other than that of LaMnO$_3$, are detected, suggesting that they have pure phase structure, and all the Ce atoms enter the framework of LaMnO$_3$ perovskite. For samples at $x \geq 0.1$, a new peak at 2θ = 28.5° that is assigned to the characteristic diffraction peak of CeO$_2$ (PDF#78-0694) appears, indicating that some Ce atoms are presented on the surface of LaMnO$_3$ as CeO$_2$ crystallizes. It is noted that the peak intensity at 2θ = 32.6° weakens with the increase in Ce amounts ($x > 0.1$), which can a result of (1) the entrance of Ce atoms decreases the crystallinity of LaMnO$_3$ due to its larger ionic radius (relative to that of La atoms) and (2) more CeO$_2$ is formed and covered on the surface of La$_{1-x}$Ce$_x$MnO$_3$, affecting the diffraction of the materials. Figure 2b shows the Raman patterns of La$_{1-x}$Ce$_x$MnO$_3$. The strong peak of 650 cm^{-1} appears for all the samples and is assigned to the LaMnO$_3$ perovskite structure [26]. For the Ce doped samples, La$_{0.9}$Ce$_{0.1}$MnO$_3$ and La$_{0.8}$Ce$_{0.2}$MnO$_3$, two new peaks, at 465 cm^{-1} and 600 cm^{-1}, appear, which are attributed to the vibration of the Ce−O bond and the defect introduction pattern caused by Ce^{3+}, respectively [27]. This suggests that the Ce atoms entered the framework of LaMnO$_3$, accompanying the formation of CeO$_2$ crystals.
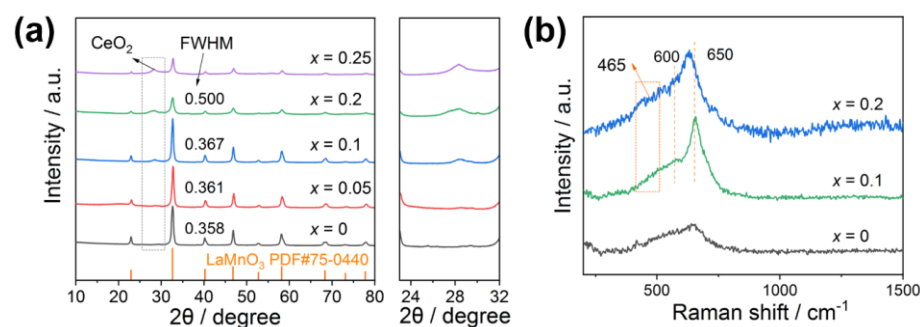
Figure 2. (**a**) XRD patterns, (**b**) Raman patterns of $La_{1-x}Ce_xMnO_3$ $(0 \leq x \leq 0.25)$ catalysts.

2.3. N_2 Physisorption Isotherms

The N_2 physisorption isotherms of $La_{1-x}Ce_xMnO_3$ catalysts are present in Figure 3, showing that all the samples have a typical IV isotherm with an H_3-type hysteresis loop, which indicates the presence of a mesoporous structure formed by stacking particles. The surface area of the samples, calculated with the BET method, are also present in the picture for convenience, which shows that the doping of Ce atoms can slightly improve the surface area, in accordance with that reported in the literature [28]. As an example, the surface area increases from 21.4 m^2/g for $LaMnO_3$ to 25.8 m^2/g for $La_{0.8}Ce_{0.2}MnO_3$. However, the surface area slightly decreases with the further increase in Ce content (e.g., $La_{0.75}Ce_{0.25}MnO_3$), due to the formation of CeO_2 phases on the surface, blocking the pores. Figure 3b shows the pore size distribution of $La_{1-x}Ce_xMnO_3$, which infers that the pore size distribution is mainly between 0–100 nm for all catalysts. $La_{0.8}Ce_{0.2}MnO_3$, $La_{0.95}Ce_{0.05}MnO_3$, and $LaMnO_3$ exhibit similar pore size distribution, but quite different CO oxidation activity, hence no direct relationship between them could be correlated. This is possible since the pore size is not the only factor affecting the catalytic activity. Other factors, such as the property of active sites, the oxidation states of metal ions, the synergistic effect between different phases, etc., should also be considered, as discussed below.
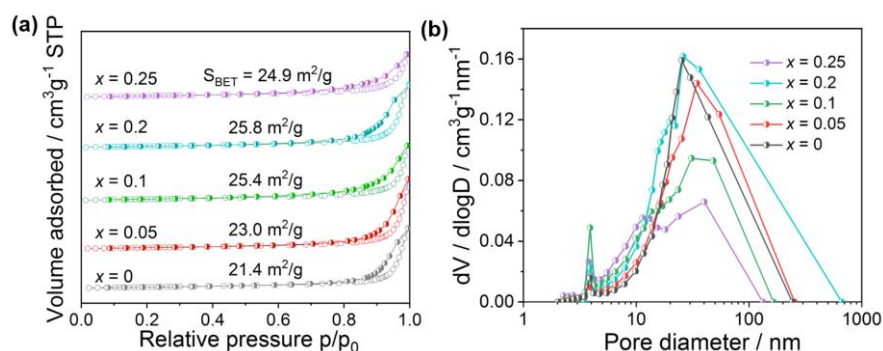

Figure 3. N_2 adsorption—desorption isotherms (**a**) and pore size distribution (**b**) of $La_{1-x}Ce_xMnO_3$ $(0 \leq x \leq 0.25)$ catalysts.

2.4. TEM Results

Figure 4 presents the TEM images of $LaMnO_3$ and $La_{0.8}Ce_{0.2}MnO_3$. Both samples exhibit disordered shape, and the particles are aggregated due to the high temperature applied in the calcination process (Figure 4a,b). From the high-resolution TEM images shown in Figure 4c, d, it is seen that $LaMnO_3$ mainly exposes the (012) crystal plane with a lattice distance of 0.386 nm, while $La_{0.8}Ce_{0.2}MnO_3$ mainly exposes the (021) crystal planes with a lattice distance of 0.258 nm. Hence, the doping of Ce atoms alters the lattice exposure of $LaMnO_3$. From the FFT pattern of $La_{0.8}Ce_{0.2}MnO_3$ (Figure 4e), (012), (021), and (122) crystal planes are observed. This indicates that $La_{0.8}Ce_{0.2}MnO_3$ is not a single exposed crystal surface, which is consistent with our previous work [18]. The mapping images of $La_{0.8}Ce_{0.2}MnO_3$ shown in Figure 4f–j show that the La, Ce, Mn, and O atoms are uniformly

distributed in the catalyst despite of the formation of CeO_2. This suggests that the CeO_2 phase is finely dispersed around the $LaMnO_3$ perovskite. This is possible since CeO_2 is formed in situ in the material by a one-pot preparation method.
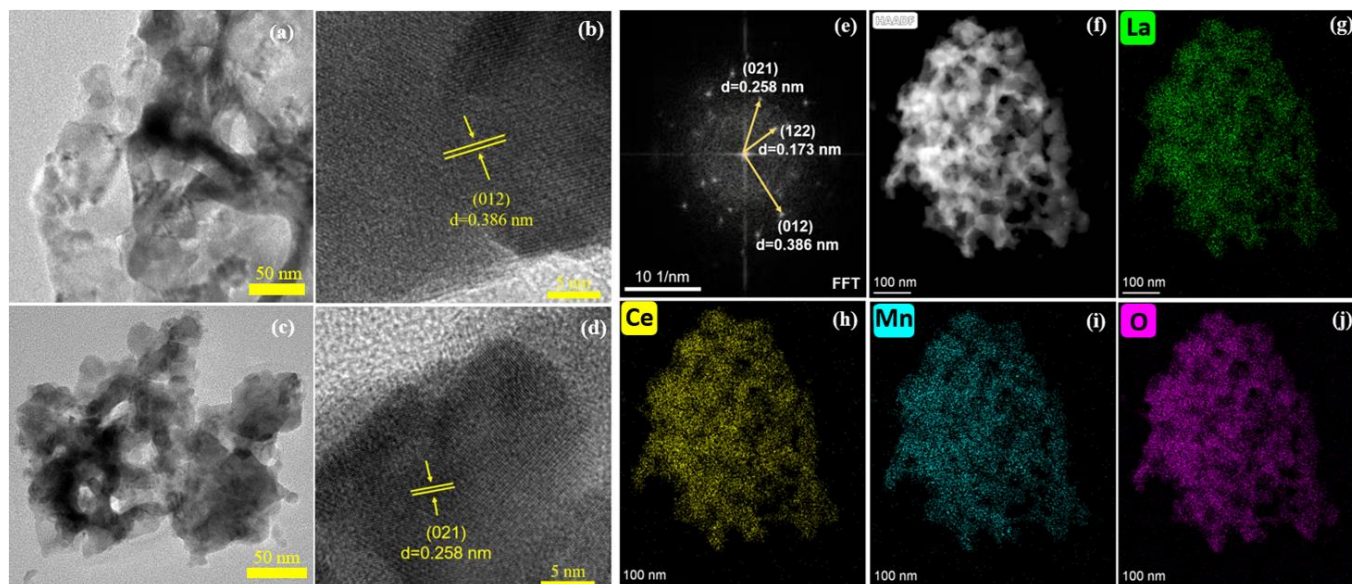

Figure 4. TEM images of (**a**,**b**) $LaMnO_3$, (**c**,**d**) $La_{0.8}Ce_{0.2}MnO_3$, (**e**) the corresponding SAED pattern and EDS images (**f**–**j**) of $La_{0.8}Ce_{0.2}MnO_3$.

2.5. XPS Results

XPS measurement is conducted to detect the surface chemistry of the samples, and the spectra are presented in Figure 5. For La 3d XPS spectra, they contain two sets of peaks that are contributed by La $3d_{3/2}$ and $3d_{5/2}$, Figure 5a. The former can be further divided into two peaks at binding energies of 854.8 eV and 850.4 eV, and the latter is divided into two peaks at binding energies of 837.9 eV and 833.5 eV, respectively. The difference between the binding energy (ΔE) of La $3d_{3/2}$ and $3d_{5/2}$ is 16.9 eV, which is similar to that of La_2O_3 (16.8 eV), as reported in the literature [29]. Hence, it can be concluded that the La cations of $LaMnO_3$ and $La_{1-x}Ce_xMnO_3$ exist in the +3 oxidation state.

Figure 5b shows the Ce 3d XPS spectra of $La_{1-x}Ce_xMnO_3$, which are composed of Ce $3d_{3/2}$ and $3d_{5/2}$ peaks, labeled as U and V in the following for convenience. For Ce $3d_{3/2}$, four peaks at binding energies of 900.4, 903.5, 907.0, and 916.0 eV can be fitted and are labeled as U_1, U_2, U_3, and U_4, respectively. Additionally, four peaks are fitted for Ce $3d_{5/2}$ at binding energies of 881.6, 882.8, 888.1, and 897.5 eV and are marked as V_1, V_2, V_3, and V_4, respectively. According to studies [30,31], the V_2 and U_2 peaks belong to the Ce^{3+} species, and V_1, V_3, V_4, U_1, U_3, and U_4 are assigned to Ce^{4+} species. From the molar ratio of $Ce^{3+}/(Ce^{3+}+Ce^{4+})$, Table 1, calculated based on the peak area of them, it can be concluded that Ce^{4+} is the main Ce species on the surface of $La_{1-x}Ce_xMnO_3$ catalysts. This can be explained by their good stability at high temperature relative to that of Ce^{3+} [32]. In addition, according to the principle of electro neutrality, it is known that the presence of more low-valence Ce^{3+} (or a higher Ce^{3+} ratio) leads to the generation of more oxygen vacancies [33]. Hence, from the change of the $Ce^{3+}/(Ce^{3+}+Ce^{4+})$ ratio listed in Table 1—$La_{0.8}Ce_{0.2}MnO_3 > La_{0.9}Ce_{0.1}MnO_3 > La_{0.75}Ce_{0.25}MnO_3$—it is concluded that the surface of $La_{0.8}Ce_{0.2}MnO_3$ contains more oxygen vacancies, and the exposed metal cations have lower coordination numbers that are beneficial to the adsorption of oxygen [34], thereby improving the catalytic activity.
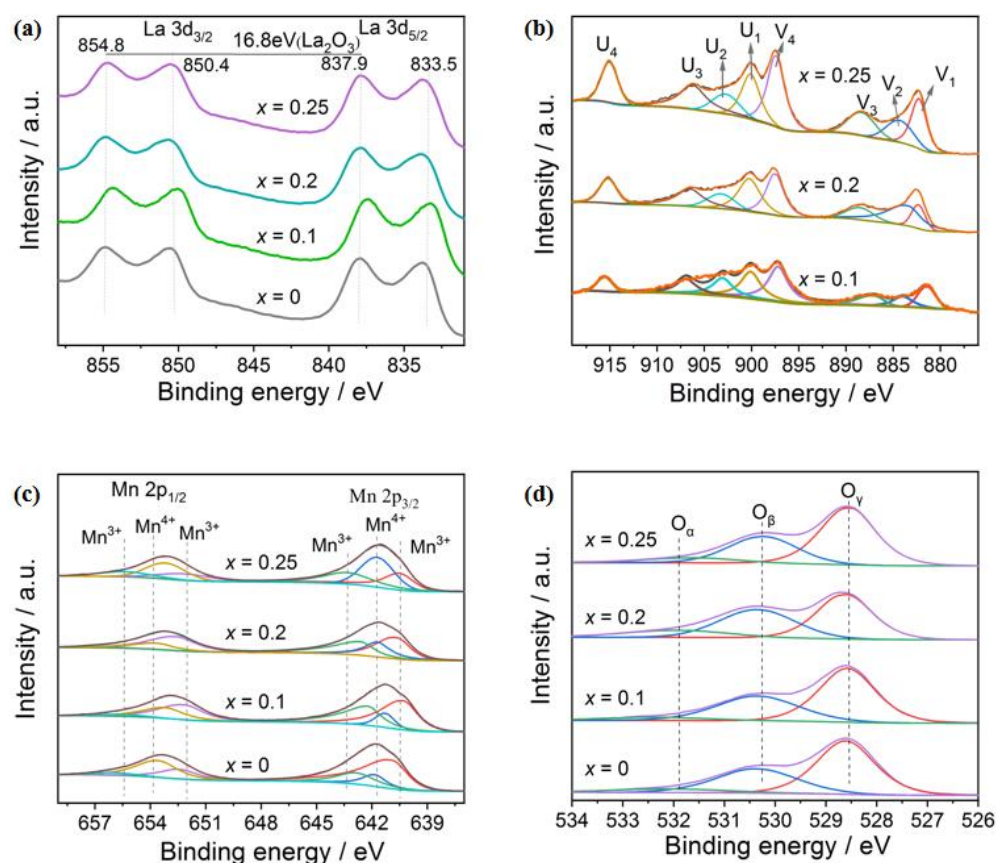
Figure 5. XPS spectra of $La_{1-x}Ce_xMnO_3$ ($0 \leq x \leq 0.25$): (**a**) La 3d; (**b**) Ce 3d; (**c**) Mn 2p; (**d**) O 1s.

The Mn 2p XPS spectra consist of two asymmetric peaks contributed by Mn $2p_{1/2}$ and Mn $2p_{3/2}$, Figure 5c. Three peaks can be fitted for them, with binding energies at 652.6, 653.6, and 656.5 eV for the Mn $2p_{1/2}$ peak and binding energies at 640.7, 641.7, and 642.6 eV for the Mn $2p_{3/2}$ peak. According to the literature [35,36], the peaks at binding energies of 640.7 and 652.6 eV are assigned to Mn^{3+} ions, and the peaks at 641.7 and 653.6 eV are attributed to Mn^{4+} ions, and those at 642.6 and 656.2 eV are satellite peaks of Mn^{3+} ions. The transformation between Mn^{3+} and Mn^{4+} species accounts for the activity of $La_{1-x}Ce_xMnO_3$ for CO oxidation. Hence, the Mn^{4+}/Mn^{3+} ratio is a crucial factor influencing the reaction rate, as it affects the reaction rate by donating/receiving electrons to/from the reactants, to accomplish a catalytic cycle. From the above results—that $La_{0.8}Ce_{0.2}MnO_3$ exhibits the best activity for the reaction (Figure 1)—it is suggested that the suitable Mn^{4+}/Mn^{3+} ratio is 0.35. A higher or lower Mn^{4+}/Mn^{3+} ratio would lead to imbalance in the oxidation and reduction steps.

The O 1s spectra of $La_{1-x}Ce_xMnO_3$ are also discussed through the deconvolution analysis, as shown in Figure 5d. Three peaks at binding energies of 528.9, 530.9, and 532.7 eV are fitted, which are assigned to lattice oxygen (O_γ), chemically adsorbed oxygen on oxygen vacancy (O_β), and adsorbed oxygen-containing groups (O_α), such as hydroxyl (OH^-) or carbonate (CO_3^{2-}) [37]. With the increase in Ce doping, the O_β/O_γ ratio of $La_{1-x}Ce_xMnO_3$ increases first, and then decreases, with the highest value (0.81) obtained at $La_{0.8}Ce_{0.2}MnO_3$, Table 2. This indicates that the $La_{0.8}Ce_{0.2}MnO_3$ catalyst possesses the most amounts of oxygen vacancy, which is believed to be the active site of oxygen adsorption and activation.

Table 2. Ratios of surface species of $La_{1-x}Ce_xMnO_3$ obtained from XPS.

Catalysts	$Ce^{3+}/(Ce^{3+} + Ce^{4+})$	Mn^{4+}/Mn^{3+}	O_β/O_γ
$LaMnO_3$	-	0.55	0.62
$La_{0.9}Ce_{0.1}MnO_3$	0.23	0.29	0.65
$La_{0.8}Ce_{0.2}MnO_3$	0.27	0.35	0.81
$La_{0.75}Ce_{0.25}MnO_3$	0.20	0.82	0.58

The change in the oxidation state of surface Mn^{4+}/Mn^{3+} and its amount of oxygen species clearly demonstrates that the Ce atoms enter the La site of $LaMnO_3$. However, the effect on different species is diverse. For the Ce species, the Ce^{3+} percentage reaches the highest at $La_{0.8}Ce_{0.2}MnO_3$, which could be attributed to the formation of interfaces between CeO_2 and $LaMnO_3$. At low Ce doping, the interfaces are less or not well formed, while at high Ce content, the amount of CeO_2 is excess and covers the surface, leading to less surface Ce^{3+} percentage. For the Mn species, the M^{4+} percentage abruptly decreases after the Ce doping, due to the presence of Ce^{4+}, which causes transformation of Mn^{4+} to Mn^{3+} according to the principle of electroneutrality. While the Mn^{4+} percentage gradually increases with the Ce doping, due to the segregation of CeO_2 and the formation of $CeO_2/LaMnO_3$ interfaces, exposing more unsaturated surface. For the O species, the Ce doping initially improves, but then decreases, the amount of oxygen vacancy. This suggests that the Ce doping induces the generation of oxygen vacancy on the surface, but the surface would be covered when too much excess CeO_2 is formed.

2.6. H₂-TPR Results

Figure 6 shows the H_2-TPR profiles of $La_{1-x}Ce_xMnO_3$ catalysts. Overall, the profiles contain two basic reduction peaks: one at the low temperature region of 250–500 °C, and the other at the high temperature region of 600–900 °C. Generally, for $LaMnO_3$ based perovskite oxides, the first region corresponds to the reduction of $Mn^{4+} \rightarrow Mn^{3+}$, and the second to the reduction of $Mn^{3+} \rightarrow Mn^{2+}$ [38]. Herein, because the temperature of the second reduction peak largely exceeds that applied in the catalytic reaction (<300 °C), we mainly analyze and discuss the low temperature reduction peak in the following.
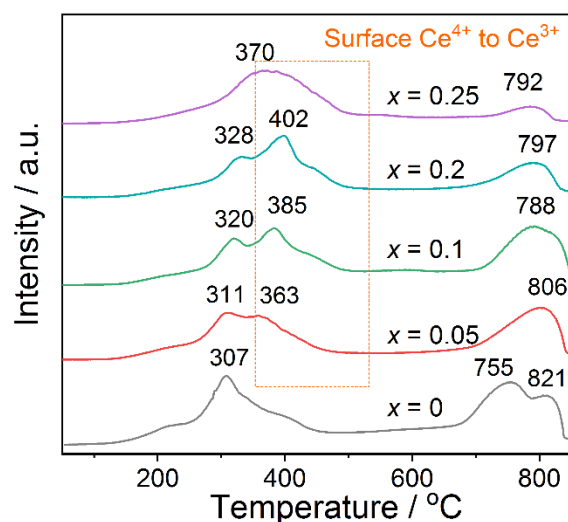
Figure 6. H_2-TPR profiles of $La_{1-x}Ce_xMnO_3$ ($0 \leq x \leq 0.25$) catalysts.

In the low temperature reduction region, one small reduction peak is observed for $LaMnO_3$, which can be attributed to the reduction of $Mn^{4+} \rightarrow Mn^{3+}$. With the addition of Ce atoms, a new peak at higher temperature (363–402 °C) appears for $La_{1-x}Ce_xMnO_3$, which can be attributed to the reduction of $Ce^{4+} \rightarrow Ce^{3+}$, as suggested in previous work [39]. The increase in reduction temperature and the strengthening of peak intensity support that

the Ce atoms are presented and involved in the reduction process. For the sample $x = 0.25$, i.e., $La_{0.75}Ce_{0.25}MnO_3$, it shows only a broad reduction peak, which could be due to the large amount of CeO_2 formed in the material. Thus, the reduction process of $Mn^{4+} \rightarrow Mn^{3+}$ is overlapped by that of $Ce^{4+} \rightarrow Ce^{3+}$.

2.7. Stability Test of $La_{0.8}Ce_{0.2}MnO_3$

Based on the above discussion, $La_{0.8}Ce_{0.2}MnO_3$ is selected as the model catalyst for stability tests, which are evaluated in two patterns: one is long-term stability tested at a setting temperature (160 °C) to see the activity changes with the reaction time; and the other is cycling stability tested by increasing/decreasing the temperature to complete a cycle to see the activity changes in each cycle. For the long-term stability, we see that the activity remains unchanged (within the uncertainty of experiment) for 30 h, Figure 7a. For the cycling stability, the activity curves are almost the same, except a slight decrease in the activity is observed at 180 °C with the increase in cycling times, Figure 7b. This indicates that the catalyst has good stability in the reaction. The reason for the slight decrease in activity at temperatures below 180 °C, with the increase in cycling time, could be that the surface of the catalyst is refilled with oxygen during the cooling process, occupying the active sites. These oxygens can be released after 180 °C, regenerating the active sites and hence the reaction activity.
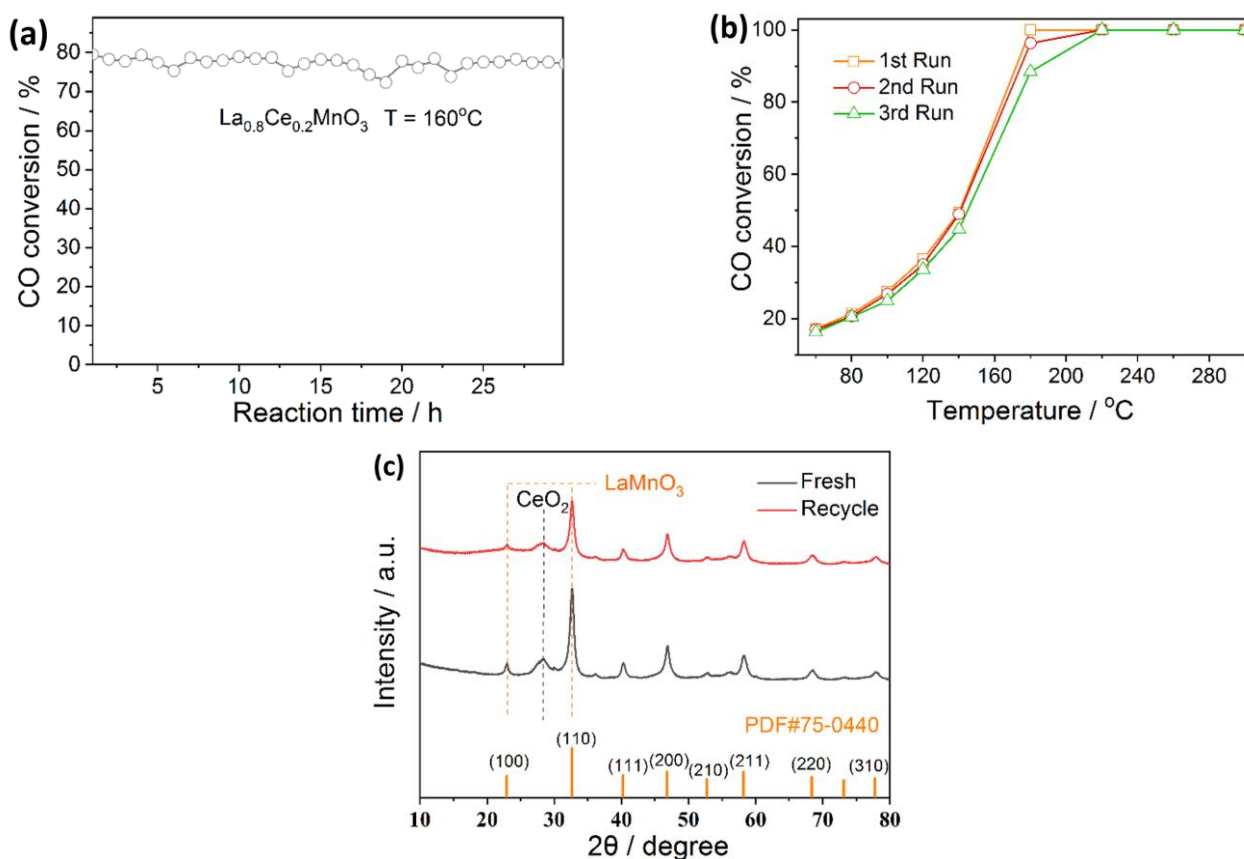

Figure 7. (**a**) Long-term and (**b**) cycling stability of $La_{0.8}Ce_{0.2}MnO_3$ for CO oxidation; (**c**) XRD patterns of the fresh and used $La_{0.8}Ce_{0.2}MnO_3$ catalyst. Reaction conditions: 0.5% CO, 6.5% O_2, and balance gas Ar.

To support the stability of $La_{0.8}Ce_{0.2}MnO_3$ in the reaction, we measured the XRD patterns of the fresh and used catalysts. Figure 7c shows that the characteristic diffraction peaks of $LaMnO_3$ and CeO_2 appear in the XRD patterns of samples before and after the reaction, which confirms that the CO oxidation process does not change the phase structure of $La_{0.8}Ce_{0.2}MnO_3$, and the catalyst has good stability in the reaction.

Hence, it is concluded that the Ce doping improves the surface area, the redox ability, and the catalytic performances of $LaMnO_3$ for CO oxidation, meanwhile preserving good stability in the reaction. The results suggest that Ce as a promotor can improve catalytic performances of perovskite oxides by inducing the formation of oxygen vacancies, the change of oxidation states of metal ions, and/or the production of synergistic effects, which could be a direction to optimize perovskite oxides for catalysis use.

3. Experimental

3.1. Catalyst's Preparation

The catalysts were synthesized by a sol–gel method using ethylene glycol and methanol mixture as the complexant and nitrates of La, Ce and Mn as the precursors, as described elsewhere [18]. Briefly, a certain amount of ethylene glycol and methanol mixed solution, with volume ratio of 3:2, was first prepared, to which $La(NO_3)_3 \bullet nH_2O$, $Mn(NO_3)_3$ and $Ce(NO_3)_3 \bullet 6H_2O$, with varied $Ce/(La + Ce)$ molar ratios ($0 \leq x \leq 0.25$), were added. The mixed solution was stirred magnetically in a water bath at 80 °C for 2 h and then dried in an oven at 100 °C for 12 h. The dried solid sample was crashed and calcined at 750 °C for 5 h in an air atmosphere (the heating rate is 2 °C/min). The obtained catalyst was marked as $La_{1-x}Ce_xMnO_3$ ($0 \leq x \leq 0.25$).

3.2. Catalyst Characterization

XRD patterns were obtained using a Rigaku Ultima IV X-ray instrument with $K\alpha$ radiation ($\lambda = 1.5418$ Å). Raman spectra were tested by LabRAM HR Evolution, using the wavelength of 532 nm. N_2 physisorption was performed on a BEISHIDE 2000PS2 instrument at −196 °C. The sample was degassed in vacuum, at 200 °C, for 5 h, before measurements. The surface area was calculated by the Brunauer−Emmett−Teller (BET) method. TEM images were observed on a JEM-2100Plus instrument. The sample was ultrasonically dispersed in an ethanol solution for several seconds before being deposited on carbon-coated copper grids for observation. XPS spectra were performed on a Thermo Scientific K-Alpha apparatus equipped with a monochromated Al $K\alpha$ X-ray source. Peak fitting was performed using the Thermo Scientific Advantage software. The binding energy was calibrated with the C1s of adventitious carbon. H_2-TPR profile was plotted on a DAS-7000 apparatus (Huasi instrument Co., Hunan, China). A 30 mg sample was treated in N_2 at 300 °C for 1 h and then cooled to room temperature (RT). Thereafter, a 10 vol% H_2/N_2 mixture was switched, with a flow rate of 20 mL/min. After reaching a stable baseline, the sample was heated from RT to 850 °C, at a heating rate of 10 °C/min, to record the profile.

3.3. Catalytic Test

The CO oxidation reaction was carried out in a fixed bed reactor. The inner diameter of the quartz fixed bed reaction tube is 6 mm, and the length is 400 mm. The simulated flue gas containing 0.5% CO and 6.5% O_2 (balanced with Ar) was passed at a total flow rate of 50 mL/min. The amount of catalyst used was 0.1 g. The catalytic activity in the temperature range of 60−300 °C was detected, and each temperature point was maintained for 30 min. The outlet gas compositions were analyzed by an online gas chromatograph. The CO conversion was calculated as below:

$$\text{CO conversion } (\%) = \frac{C_{(CO_{in})} - C_{(CO_{out})}}{C_{(CO_{in})}} \times 100\%$$

where $C_{(CO_{in})}$ and $C_{(CO_{out})}$ are the CO concentration at the inlet and outlet, respectively.

4. Conclusions

In summary, $La_{1-x}Ce_xMnO_3$ catalysts for CO catalytic oxidation are successfully prepared by the sol–gel method, and the effect of Ce doping on the rection is investigated. At low Ce doping ($x < 0.1$), the Ce atoms enter the $LaMnO_3$ perovskite structure, but at high Ce doping ($x \geq 0.1$), part of Ce stays on the surface of $LaMnO_3$ as CeO_2 crystalline.

The La$_{0.8}$Ce$_{0.2}$MnO$_3$ catalyst exhibits disordered shape, and its particles are aggregated. XPS results show that, at x = 0.2, the sample, i.e., La$_{0.8}$Ce$_{0.2}$MnO$_3$, possesses the highest surface Ce^{3+}/(Ce^{3+} + Ce^{4+}) and O$_\beta$/O$_\gamma$ molar ratio, implying the generation of more oxygen vacancies on the surface, which is believed to be the active site of O$_2$ adsorption and activation. As a result, after the doping of Ce atoms, the activity of La$_{1-x}$Ce$_x$MnO$_3$ shows a trend of initial increase and then decrease. La$_{0.8}$Ce$_{0.2}$MnO$_3$ shows the highest activity for CO oxidation among the investigated La$_{1-x}$Ce$_x$MnO$_3$ samples, with 100% CO conversion obtained at 180 °C. Moreover, the material possesses good long-term and cycling stability in the reaction, and the structure remain unchanged for the fresh and used La$_{0.8}$Ce$_{0.2}$MnO$_3$, as detected by the XRD patterns.

References

1. Konsolakis, M.; Yentekakis, I.V. Insight into the role of electropositive promoters in emission control catalysis: An in situ drifts study of NO reduction by C$_3$H$_6$ over Na-promoted Pt/Al$_2$O$_3$ catalysts. *Top. Catal.* **2013**, *56*, 165–171. [CrossRef]
2. Altass, H.M.; Morad, M.; Khder, A.E.-R.S.; Mannaa, M.A.; Jassas, R.S.; Alsimaree, A.A.; Ahmed, S.A.; Salama, R.S. Enhanced catalytic activity for CO oxidation by highly active Pd nanoparticles supported on reduced graphene oxide/copper metal organic framework. *J. Taiwan Inst. Chem. Eng.* **2021**, *128*, 194–208. [CrossRef]
3. Brook, R.D.; Franklin, B.; Cascio, W.; Hong, Y.; Howard, G.; Lipsett, M.; Luepker, R.; Mittleman, M.; Samet, J.; Smith, S.C., Jr.; et al. Air pollution and cardiovascular disease: A statement for healthcare professionals from the Expert Panel on Population and Prevention Science of the American Heart Association. *Circulation* **2004**, *109*, 2655–2671. [CrossRef] [PubMed]
4. Wang, S.; Xu, X.L.; Xiao, P.; Zhu, J.J.; Liu, X.Y. Cooperative effect between copper species and oxygen vacancy in Ce$_{0.7-x}$Zr$_x$Cu$_{0.3}$O$_2$ catalysts for carbon monoxide oxidation. *Front. Chem. Sci. Eng.* **2021**, *15*, 1524–1536. [CrossRef]
5. Alshorifi, F.T.; Ali, S.L.; Salama, R.S. Promotional synergistic effect of Cs-Au NPs on the performance of Cs-Au/MgFe$_2$O$_4$ catalysts in catalysis 3,4-Dihydropyrimidin-2(1H)-Ones and degradation of RhB Dye. *J. Inorg. Organomet. Polym. Mater.* **2022**, *32*, 3765–3776. [CrossRef]
6. Eichhorn, L.; Thudium, M.; Juttner, B. The diagnosis and treatment of carbon monoxide poisoning. *Dtsch. Arztebl. Int.* **2018**, *115*, 863–870. [CrossRef] [PubMed]
7. Li, X.N.; Wang, L.N.; Mou, L.H.; He, S.G. Catalytic CO oxidation by gas-phase metal oxide clusters. *J. Phys. Chem. A* **2019**, *123*, 9257–9267. [CrossRef] [PubMed]
8. López-Suárez, F.E.; Bueno-López, A.; Illán-Gómez, M.J.; Trawczynski, J. Potassium-copper perovskite catalysts for mild temperature diesel soot combustion. *J. Mol. Catal. A Chem.* **2014**, *485*, 214–221. [CrossRef]
9. Zhang, C.; Wang, C.; Zhan, W.; Guo, Y.; Guo, Y.; Lu, G.; Baylet, A.; Giroir-Fendler, A. Catalytic oxidation of vinyl chloride emission over LaMnO$_3$ and LaB$_{0.2}$Mn$_{0.8}$O$_3$ (B=Co, Ni, Fe) catalysts. *Appl. Catal. B Environ.* **2013**, *129*, 509–516. [CrossRef]
10. Zhu, J.; Li, H.; Zhong, L.; Xiao, P.; Xu, X.; Yang, X.; Zhao, Z.; Li, J. Perovskite oxides: Preparation, characterizations, and applications in heterogeneous catalysis. *ACS Catal.* **2014**, *4*, 2917–2940. [CrossRef]
11. Royer, S.; Alamdari, H.; Duprez, D.; Kaliaguine, S. Oxygen storage capacity of La$_{1-x}$A$'_x$BO$_3$ perovskites (with A$'$=Sr, Ce; B=Co, Mn)-relation with catalytic activity in the CH$_4$ oxidation reaction. *Appl. Catal. B Environ.* **2005**, *58*, 273–288. [CrossRef]
12. Ivanov, D.V.; Sadovskaya, E.M.; Pinaeva, L.G.; Isupova, L.A. Influence of oxygen mobility on catalytic activity of La–Sr–Mn–O composites in the reaction of high temperature N$_2$O decomposition. *J. Catal.* **2009**, *267*, 5–13. [CrossRef]
13. Zhou, Y.; Wang, Z.; Liu, C. Perspective on CO oxidation over Pd-based catalysts. *Catal. Sci. Technol.* **2015**, *5*, 69–81. [CrossRef]
14. Al Soubaihi, R.; Saoud, K.; Dutta, J. Critical review of low-temperature CO oxidation and hysteresis phenomenon on heterogeneous catalysts. *Catalysts* **2018**, *8*, 660. [CrossRef]
15. Nakamura, T.; Misono, M.; Yoneda, Y. Reduction-oxidation and catalytic properties of perovskite-type mixed oxide catalysts (La$_{1-x}$Sr$_x$CoO$_3$). *Chem. Lett.* **1981**, *10*, 1589–1592. [CrossRef]
16. Myung, C.-L.; Jang, W.; Kwon, S.; Ko, J.; Jin, D.; Park, S. Evaluation of the real-time de-NO$_x$ performance characteristics of a LNT-equipped Euro-6 diesel passenger car with various vehicle emissions certification cycles. *Energy* **2017**, *132*, 356–369. [CrossRef]

17. Alifanti, M.; Florea, M.; Pârvulescu, V.I. Ceria-based oxides as supports for LaCoO$_3$ perovskite catalysts for total oxidation of VOC. *Appl. Catal. B Environ.* **2007**, *70*, 400–405. [CrossRef]

18. Wang, S.; Xu, X.; Zhu, J.; Tang, D.; Zhao, Z. Effect of preparation method on physicochemical properties and catalytic performances of LaCoO$_3$ perovskite for CO oxidation. *J. Rare Earths* **2019**, *37*, 970–977. [CrossRef]

19. Zhu, X.; Zhang, S.; Yang, Y.; Zheng, C.; Zhou, J.; Gao, X.; Tu, X. Enhanced performance for plasma-catalytic oxidation of ethyl acetate over La$_{1-x}$Ce$_x$CoO$_{3+\delta}$ catalysts. *Appl. Catal. B Environ.* **2017**, *213*, 97–105. [CrossRef]

20. Xiang, X.P.; Zhao, L.H.; Teng, B.T.; Lang, J.J.; Hu, X.; Li, T.; Fang, Y.A.; Luo, M.F.; Lin, J.J. Catalytic combustion of methane on La$_{1-x}$Ce$_x$FeO$_3$ oxides. *Appl. Surf. Sci.* **2013**, *276*, 328–332. [CrossRef]

21. Mathieu-Deremince, V.; Nagy, J.B.; Verbist, J.J. Structure and catalytic activity of mixed oxides of perovskite structure. *Stud. Surf. Sci. Catal.* **1995**, *96*, 393–404.

22. Zhou, H.; Wu, Q.; Qi, B. Facile one-step flame synthesis of La$_{1-x}$Sr$_x$MnO$_3$ nanoparticles for CO catalytic oxidation. *J. Chem.* **2021**, *2021*, 9472008. [CrossRef]

23. Huang, X.; Niu, P.; Pan, H.; Shang, X. Micromorphological control of porous LaMnO$_3$ and LaMn$_{0.8}$Fe$_{0.2}$O$_3$ and its catalytic oxidation performance for CO. *J. Solid State Chem.* **2018**, *265*, 218–226. [CrossRef]

24. Cimino, S.; Lisi, L.; De Rossi, S.; Faticanti, M.; Porta, P. Methane combustion and CO oxidation on LaAl$_{1-x}$Mn$_x$O$_3$ perovskite-type oxide solid solutions. *Appl. Catal. B Environ.* **2003**, *43*, 397–406. [CrossRef]

25. Russo, N.; Fino, D.; Saracco, G.; Specchia, V. Promotion effect of Au on perovskite catalysts for the regeneration of diesel particulate filters. *Catal. Today* **2008**, *137*, 306–311. [CrossRef]

26. Abrashev, M.V.; Litvinchuk, A.P.; Iliev, M.N.; Meng, R.L.; Popov, V.N.; Ivanov, V.G.; Chakalov, R.A.; Thomsen, C. Comparative study of optical phonons in the rhombohedrally distorted perovskites LaAlO$_3$ and LaMnO$_3$. *Phys. Rev. B* **1999**, *59*, 4146–4153. [CrossRef]

27. Zhou, Y.; Ren, S.; Yang, J.; Liu, W.; Su, Z.; Chen, Z.; Wang, M.; Chen, L. Effect of oxygen vacancies on improving NO oxidation over CeO$_2$ [32] and [17] facets for fast SCR reaction. *J. Environ. Chem. Eng.* **2021**, *9*, 106218. [CrossRef]

28. Guo, X.; Meng, M.; Dai, F.; Li, Q.; Zhang, Z.; Jiang, Z.; Zhang, S.; Huang, Y. NO$_x$-assisted soot combustion over dually substituted perovskite catalysts La$_{1-x}$K$_x$Co$_{1-y}$Pd$_y$O$_{3-\delta}$. *Appl. Catal. B Environ.* **2013**, *142–143*, 278–289. [CrossRef]

29. Alifanti, M.; Kirchnerova, J.; Delmon, B. Effect of substitution by cerium on the activity of LaMnO$_3$ perovskite in methane combustion. *J. Mol. Catal. A Chem.* **2003**, *245*, 231–244. [CrossRef]

30. Peng, Y.; Wang, C.; Li, J. Structure-activity relationship of VO$_x$/CeO$_2$ nanorod for NO removal with ammonia. *Appl. Catal. B Environ.* **2014**, *144*, 538–546. [CrossRef]

31. Bêche, E.; Charvin, P.; Perarnau, D.; Abanades, S.; Flamant, G. Ce 3d XPS investigation of cerium oxides and mixed cerium oxide (Ce$_x$Ti$_y$O$_z$). *Surf. Interface Anal.* **2008**, *40*, 264–267. [CrossRef]

32. Sakthivel, T.S.; Reid, D.L.; Bhatta, U.M.; Möbus, G.; Sayle, D.C.; Seal, S. Engineering of nanoscale defect patterns in CeO$_2$ nanorods via ex situ and in situ annealing. *Nanoscale* **2015**, *7*, 5169–5177. [CrossRef] [PubMed]

33. Holgado, J.P.; Munuera, G.; Espinós, J.P.; González-Elipe, A.R. XPS study of oxidation processes of CeO$_x$ defective layers. *Appl. Surf. Sci.* **2000**, *158*, 164–171. [CrossRef]

34. Liu, X.; Zhou, K.; Wang, L.; Wang, B.; Li, Y. Oxygen vacancy clusters promoting reducibility and activity of ceria nanorods. *J. Am. Chem. Soc.* **2009**, *131*, 3140–3141. [CrossRef]

35. Hammami, R.; Aïssa, S.B.; Batis, H. Effects of thermal treatment on physico-chemical and catalytic properties of lanthanum manganite LaMnO$_{3+y}$. *J. Mol. Catal. A Chem.* **2009**, *353*, 145–153. [CrossRef]

36. Magkoev, T.T.; Zaalishvili, V.B.; Burdzieva, O.G.; Tuaev, G.E.; Grigorkina, G.S. Interaction of Co, Mn, and Fe atoms with calcite: An X-ray photoelectron spectroscopy study. *Geochem. Int.* **2019**, *57*, 98–103. [CrossRef]

37. Fierro, J.L.G.; Tejuca, L.G. Non-stoichiometric surface behaviour of LaMO$_3$ oxides as evidenced by XPS. *Appl. Surf. Sci.* **1987**, *27*, 453–457. [CrossRef]

38. Lisi, L.; Bagnasco, G.; Ciambelli, P.; De Rossi, S.; Porta, P.; Russo, G.; Turco, M. Perovskite-type oxides: II. redox properties of LaMn$_{1-x}$Cu$_x$O$_3$ and LaCo$_{1-x}$Cu$_x$O$_3$ and methane catalytic combustion. *J. Solid State Chem.* **1999**, *146*, 176–183. [CrossRef]

39. Zhu, J.; Zhao, Y.; Tang, D.; Zhao, Z.; Carabineiro, S.A.C. Aerobic selective oxidation of alcohols using La$_{1-x}$Ce$_x$CoO$_3$ perovskite catalysts. *J. Catal.* **2016**, *340*, 41–48. [CrossRef]